



OPEN

Cryo-EM structure of SKP1-SKP2-CKS1 in complex with CDK2-cyclin A-p27KIP1

Rhianna J. Rowland¹, Richard Heath¹, Daniel Maskell², Rebecca F. Thompson^{2,4}, Neil A. Ranson², James N. Blaza³, Jane A. Endicott^{1✉}, Martin E. M. Noble¹ & Marco Salamina^{1,5✉}

p27KIP1 (cyclin-dependent kinase inhibitor 1B, p27) is a member of the CIP/KIP family of CDK (cyclin dependent kinase) regulators that inhibit cell cycle CDKs. p27 phosphorylation by CDK1/2, signals its recruitment to the SCF^{SKP2} (S-phase kinase associated protein 1 (SKP1)-cullin-SKP2) E3 ubiquitin ligase complex for proteasomal degradation. The nature of p27 binding to SKP2 and CKS1 was revealed by the SKP1-SKP2-CKS1-p27 phosphopeptide crystal structure. Subsequently, a model for the hexameric CDK2-cyclin A-CKS1-p27-SKP1-SKP2 complex was proposed by overlaying an independently determined CDK2-cyclin A-p27 structure. Here we describe the experimentally determined structure of the isolated CDK2-cyclin A-CKS1-p27-SKP1-SKP2 complex at 3.4 Å global resolution using cryogenic electron microscopy. This structure supports previous analysis in which p27 was found to be structurally dynamic, transitioning from disordered to nascent secondary structure on target binding. We employed 3D variability analysis to further explore the conformational space of the hexameric complex and uncovered a previously unidentified hinge motion centred on CKS1. This flexibility gives rise to open and closed conformations of the hexameric complex that we propose may contribute to p27 regulation by facilitating recognition with SCF^{SKP2}. This 3D variability analysis further informed particle subtraction and local refinement approaches to enhance the local resolution of the complex.

Abbreviations

CBF	Cyclin-box fold
CDK	Cyclin-dependent kinase
CKI	Cyclin-dependent kinase inhibitor
CKS1	Cyclin-dependent kinases regulatory subunit 1
LRR	Leucine rich repeats
RMSD	Root mean square deviation
SEC	Size exclusion chromatography
SKP	S-phase kinase associated protein
FSC	Fourier shell correlation
CTF	Contrast transfer function

The cyclin-dependent protein kinases (CDKs), CDK1, CDK2 and CDK4/6 coordinate events of the eukaryotic cell cycle to ensure genome and cell integrity is maintained through generations¹⁻³. Activation of CDK4/6-cyclin D complexes is a response to mitogenic signals early in G1, and cell cycle progression is sustained through late G1 and S-phase by CDK2 partnered first by cyclin E and then cyclin A. CDK1-cyclin B is also reported to be active during S-phase⁴ and the activity of CDK1 bound to cyclins A and B guides the cell through G2 into mitosis to ensure its timely completion. The CDK-cyclin module is regulated by reversible phosphorylation and association with a range of protein inhibitors and activators that modulate activity, substrate preferences and

¹Translational and Clinical Research Institute, Newcastle University Centre for Cancer, Newcastle University, Paul O'Gorman Building, Framlington Place, Newcastle Upon Tyne NE2 4HH, UK. ²Astbury Centre for Structural Molecular Biology, School of Molecular and Cellular Biology, University of Leeds, Leeds LS2 9JT, UK. ³Department of Chemistry, York Structural Biology Laboratory and York Biomedical Research Institute, University of York, Heslington YO10 5DD, York, UK. ⁴Present address: Life Sciences Electron Microscopy, Thermo Fisher Scientific, Leeds, UK. ⁵Present address: Evotec (UK) Ltd., Milton, Abingdon OX14 4RZ, UK. ✉email: jane.endicott@ncl.ac.uk; marco.salamina@evotec.com

intracellular location (reviewed in^{5,6}). Their timely destruction by the ubiquitin proteasome system is essential to CDK control of the cell cycle, and their selection is dependent on a number of substrate-specific E3 ligases⁷. p27KIP1 (cyclin-dependent kinase inhibitor 1B, p27) is a member of the CIP/KIP family of CDK regulators that inhibit cell cycle CDKs⁸. p27 is also a CDK4/6-selective assembly factor that promotes association with D-cyclins^{8–15}. A variety of signals increase p27 levels to cause growth arrest, including cytokines, such as transforming growth factor β (TGF β)^{16,17} and interferon- γ (IFN- γ)¹⁸, and inducers of differentiation such as vitamin D3 and retinoic acid¹⁹. In contrast, low p27 levels are commonly identified in cancer and associated with poor prognosis^{20,21}. p27 is degraded via the ubiquitin proteasome system^{22,23}, where phosphorylation at Thr187 by CDK1/2 signals its recruitment to the S-phase kinase associated protein 1 (SKP1)-cullin-SKP2 E3 ubiquitin ligase complex SCF^{SKP2}^{24–31}. Though best characterised as E3 subunits, SKP1 and SKP2 were initially identified as part of a pentameric CDK2-cyclin A-CKS1-SKP1-SKP2 complex^{32–34}. Notably, p27 bound to a CDK-cyclin module is the SCF^{SKP2} substrate and unusually the binding site for phosphorylated p27 is contributed by both SKP2 and the accessory protein, CKS1^{26,35–38}. The nature of this interaction was revealed through a SKP1-SKP2-CKS1-p27 phosphopeptide crystal structure³⁸. Given its cellular importance in regulating p27, a predicted model for the CDK2-cyclin A-CKS1-p27-SKP1-SKP2 complex was proposed by overlaying independent structures of CDK2-cyclin A-p27³⁹ and SKP1-SKP2-CKS1-p27 peptide⁴⁰. However, definitive experimental evidence for this architecture has not yet been reported.

Here we report an experimentally determined structure of the isolated CDK2-cyclin A-CKS1-p27-SKP1-SKP2 complex using cryogenic electron microscopy (cryo-EM). At a global resolution of 3.4 Å (Fourier Shell Correlation (FSC) 0.143 cut-off), we provide structural analyses of the overall quaternary architecture and interactions that underpin this complex. The structure is in broad agreement with the octameric CUL1-RBX1-SKP1-SKP2-CKSHS1-cyclin A-CDK2-p27 complex (PDB **7B5R**) which was recently determined by cryo-EM as a focussed refined sub-complex of the full SCF-RBR E3-E3 super-assembly. We further enhanced our EM map of the hexameric complex through particle subtraction and local refinement to reveal additional structural features. 3D variability analysis also uncovered a significant hinge motion centred on CKS1, which gives rise to open and closed conformations of the complex. We speculate this motion may contribute to ubiquitin-mediated degradation of p27 by facilitating substrate recognition with the SKP2 recognition motif of SCF^{SKP2}.

Results and discussion

The structure of the CDK2-cyclin A-CKS1-SKP1-SKP2-p27 complex. Following screening by negative stain transmission electron microscopy, the hexameric complex was imaged by cryo-EM and refined to a global resolution of 3.4 Å (FSC 0.143) (Fig. 1, Supplementary Figs. S1–S4, Supplementary Table S1, PDB ID **8BYA**, EMD-**16325**). The data processing workflow is described in Supplementary Figs. S2 and S3. In summary, an initial non-biased particle set was picked using blob picker and used to generate 2D classes that were lowpass filtered to 20 Å (to reduce template bias) as templates for picking. An ab-initio 3D reconstruction was generated and used to create new 2D templates for further picking. Template picked particles were subjected to heterogeneous refinement using three 3D classes, with refinement of the best class (136,325 particles) yielding the final 3D reconstruction at 3.4 Å. An initial model for the hexameric complex was generated in UCSF ChimeraX^{41,42} by rigid body docking CDK2-cyclinA-p27 (PDB **1JSU**) and SKP1-SKP2-CKS1-p27 (PDB **2AST**) to give an initial model-to-map fit CCmask = 0.49. The fitting of the model to the EM map was improved (CCmask = 0.73) using real-space refinement⁴³ in Phenix and manual model building in COOT⁴⁴ (RMSD = 2.3 of all residues between

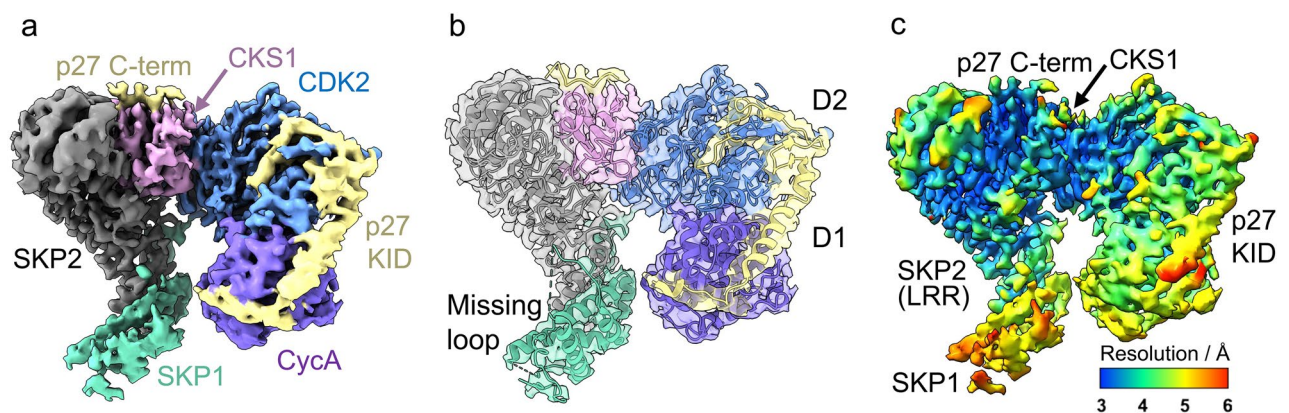


Figure 1. 3.4 Å Cryo-EM map of the hexameric SKP1-SKP2-CKS1-CDK2-cyclin A-p27 complex. (a) 3.4 Å cryo-EM map (PDB **8BYA**, EMD-**16325**) into which the full hexameric complex, comprised of SKP1 (green), SKP2 (grey), CKS1 (pink), CDK2 (blue), cyclin A (purple) and p27 (yellow), was fitted and refined using starting models PDB **2AST** and **1JSU**. (b) The refined model shows domain 1 (D1) and the helical linker domain of the N-term kinase inhibitory domain (KID) of p27 wrapping around cyclin A and engaging with the RxL binding motif whilst domain 2 (D2) extends over CDK2 towards the activation segment. The C-terminal domain of p27 lies over CKS1. (c) Local resolution analysis of the hexameric complex revealing highest resolution within SKP2(LRR)-CKS1 core (~3–3.5 Å) and lowest resolution (~5–6 Å) in the outer region of the p27 KID and SKP1.

initial and refined model). This refinement left SKP2 and CKS1 relatively unchanged compared to PDB [2AST](#), whilst moderate changes to the SKP1 domain and conformation of p27 KID bound to CDK2-Cyclin A were required (Supplementary Fig. S4c, described in more detail below).

The EM map covers the full-length of CDK2 and CKS1, and the expressed residues of cyclin A (174–432) that compose the tandem cyclin box folds. SKP1, SKP2 and p27 were expressed as full-length proteins but their structures could not be fully modelled. SKP1 has two disordered loop regions at residues 31–41 (loop 1) and 64–79 (loop 2), whilst the SKP2 structure starts at Val95 and includes the F-box (residues 109–151), leucine rich repeats (LRR, residues 151–402) and C-terminal tail (residues 402–419).

Previous studies have indicated that the N-terminus of SKP2 binds to cyclin A⁴⁵. However, this interaction is known to be mutually exclusive of p27 binding and a model in which p27 and SKP2 both engage with the cyclin A RxL site, precluding simultaneous binding in this region, has been proposed^{46,47}. Consequently, we do not observe this interaction in the hexameric complex. The lack of density for the N-terminal SKP2 residues 1–94 suggests it may be disordered in this complex. In the case of p27, the kinase inhibitory domain (KID, residues 25–93) and C-terminal sequence surrounding the phosphorylated Thr187 residue (residues 181–190) were modelled but the linking residues (94–180) were not visible (Fig. 1b). Equivalent disordered regions were noted in the octameric complex (PDB [7B5R](#)⁴⁸).

The local resolution of the complex ranges 3–6 Å, with the highest resolution (~3 Å) observed in the LRR of SKP2 and the CKS1 junction (Fig. 1c). In contrast, the poorest resolution (~5–6 Å) is observed within SKP1. SKP1 has previously been crystallised in two conformations (compare PDB [1FQV](#) and [1FS2](#)⁴⁹) and shows dynamic behaviour which appears important to its function⁵⁰. Such flexibility will likely be preserved in the cryo-EM analysis, therefore, the lower resolution reported for this domain is unsurprising. The outer region of domain 1 (D1, residues 26–37) and the linker helix domain (residues 38–59) of the p27 KID is also reported at a resolution of ~5 Å (Fig. 1b,c). This region of p27 binds to cyclin A but is known to be flexible^{51,52}. Despite this flexibility, the resolution was sufficient to model the helical backbone of the KID wrapping around cyclin A and engaging with the RxL binding motif (Fig. 1b). The resolution of p27 improves to ~4 Å across domain 2 (D2, residues 60–88) as it extends towards the Thr160-phosphorylated activation segment of CDK2 (residues 145–172, between DFG and APE motifs) (Fig. 1b,c). In accordance with the comparatively higher resolution of CKS1, the bound C-terminal domain of p27 (residues 181–190) was modelled to an improved resolution of ~3.5–4.0 Å (Fig. 1c), revealing density for Thr187 phosphorylation (discussed below and illustrated in Fig. 2e,f).

The resolution of this hexameric reconstruction permitted structural analysis of the individual proteins within the full complex using existing crystal structures of CDK2-cyclinA-p27 (PDB [1JSU](#)³⁹) and SKP1-SKP2-CKS1-p27 (PDB [2AST](#)³⁸) as starting models. Whilst these crystal structures can be overlaid to generate a predicted model, the cryo-EM complex presented here provides the first experimentally determined structure of the isolated CDK2-cyclin A-CKS1-p27-SKP1-SKP2 complex. This structure serves as a comparison with the octameric CUL1-RBX1-SKP1-SKP2-CKSHS1-CyclinA-CDK2-p27 complex (PDB [7B5R](#)⁴⁸) which was recently solved by cryo-EM, not from the isolated octameric complex but following focussed refinement of the SCF-RBR E3-E3 super-assembly complex (PDB [7B5L](#)⁴⁸).

CKS1 binds CDK2, SKP2 and p27. The interaction between CDK2 and CKS1 is entirely consistent with the CKS1-CDK2 crystal structure⁵³ (PDB [1BUH](#)), in which CKS1 interacts exclusively with the C-terminal lobe of CDK2. This interaction is underpinned by one loop of CKS1 (residues 58–64), which protrudes into a groove on the surface of CDK2 (Fig. 2a,b). At this interface, the side chain of CKS1 Glu63 hydrogen bonds with the backbone of CDK2 Glu208, whilst the backbone of CKS1 Ile59 forms a hydrogen bond to the side chain of CDK2 Lys23.

CKS1 also associates with the LRR of SKP2, and the resolution of the EM map in this region was sufficient to model side chains and validate the interactions against the SKP1-SKP2-CKS1-p27 crystal structure (PDB [2AST](#)³⁸). At the SKP2-CKS1 interface, a cluster of CKS1 residues form a hydrophobic pocket in which SKP2 Phe393 and His392 bind to stabilize the C-terminal loop (Fig. 2c,d). We previously demonstrated the importance of Phe393 in facilitating CKS1 binding by mutagenizing this residue to a Gly-Ser pair which compromised the interaction⁴⁶.

CKS1 also binds the C-terminal phospho-peptide of p27. Unfortunately, the flexible nature of p27 prevented modelling of the full sequence, however, C-terminal residues 181–190 including the phosphorylated Thr187 residue were solved to 3.5–4.0 Å. This C-terminal peptide lies over the SKP2-CKS1 junction, where the phosphorylated Thr187 sidechain protrudes into a small, positively charged pocket formed by CKS1 Tyr8, Lys11, Arg20, Ser51, Trp54 and Arg71 (Fig. 2e,f). Analysis of the CKS1 surface hydrophobicity profile also identifies a role for p27 Pro188, which stacks on top of CKS1 Tyr8 and is wedged by CKS1 Gln5 and Gln49 to provide a linkage to CKS1 whilst constraining p27 conformation through its intrinsic peptide angles (Fig. 2e,f). Whilst PDB [2AST](#) reports the p27 C-terminal peptide lying flat over the SKP2-CKS1 junction, our density suggests a more condensed, potentially helical conformation.

Engagement of the p27 KID with cyclin A and CDK2. Analysis of the p27 KID (residues 25–59) allowed us to model p27 engaging with the RxL binding motif of cyclin A and follow its path towards the CDK2 activation segment, as reported in the CDK2-cyclinA-p27 crystal structure (PDB [1JSU](#)³⁹). The N-terminal coil of p27 (D1), containing the CIP/KIP conserved Leu32-Phe33-Gly34 (LFG) sequence starts at Pro26 and is rigidified by intramolecular hydrogen bonds between Cys29 and Pro26, and between Ser27 and Arg30. This rigid coil binds in a shallow groove on the surface of the cyclin box fold (N-CBF) (Fig. 3a) and is stabilised by various hydrogen bonds; p27 Ala28, Arg30 and Asn31 hydrogen bond with cyclin A Trp218, Glu220 and Gln254 respectively. The conserved LFG sequence sits in a deeper, more hydrophobic groove formed by cyclin A Ile213,

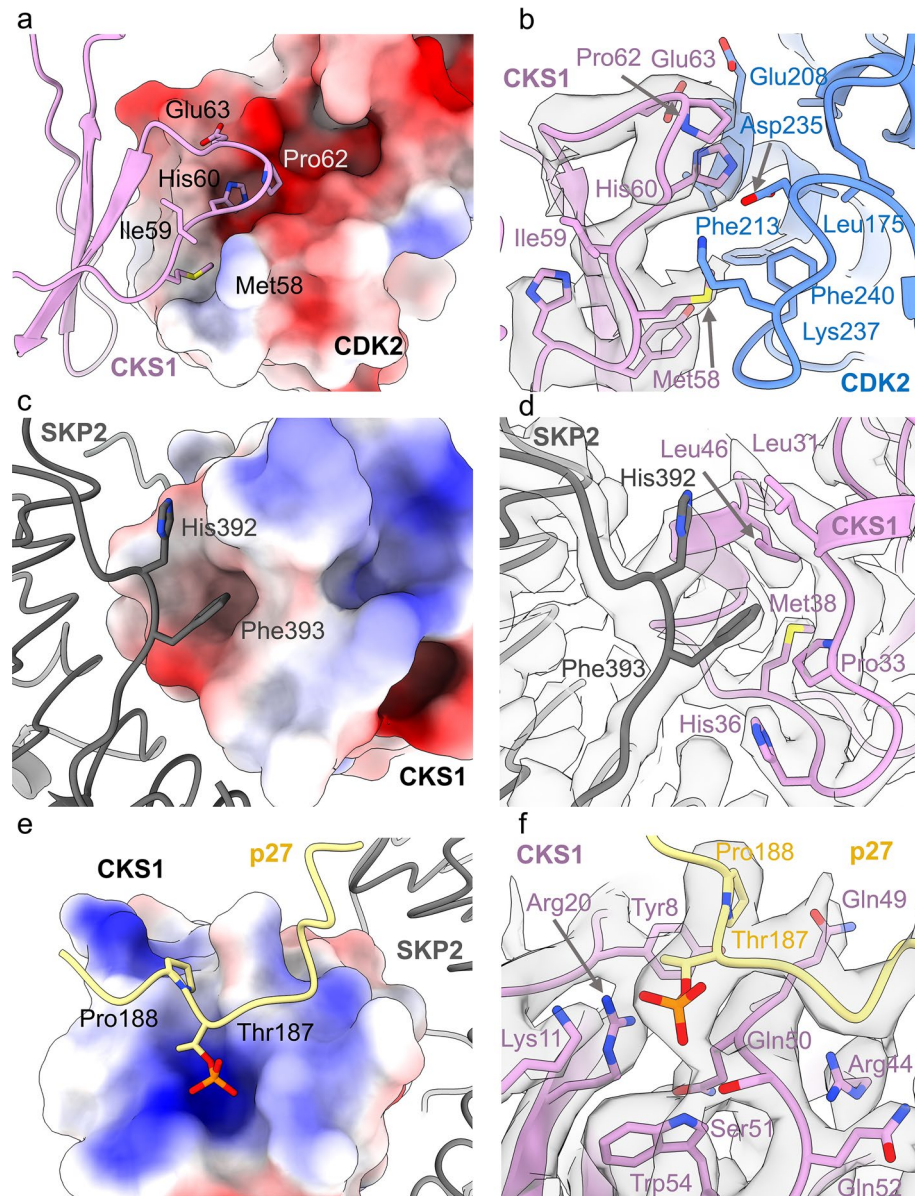


Figure 2. Interaction of CKS1 with CDK2, SKP2 and p27. **(a,b)** Interface between CKS1 (pink) and CDK2 (blue). **(a)** Electrostatic surface potential of CDK2 showing the narrow groove in which CKS1 residues Met58-Glu63 bind. **(b)** Ribbon diagram of CDK2-CKS1 interface highlighting the CDK2 residues that form the surface groove (Lys237, Phe240, Phe213, Asp235, Leu175) and density (at 8.8σ , threshold 0.337) for the interacting residues of CKS1, notably His60 and Pro62. **(c,d)** Interface between SKP2 (grey) and CKS1 (pink). **(c)** Electrostatic surface potential of CKS1 depicting the hydrophobic pocket in which SKP2 Phe393 binds **(d)** Ribbon diagram of SKP2-CKS1 interface showing density (at 8.8σ , threshold 0.406) for the binding of SKP2 Phe393 and His392 **(e,f)** Binding of p27 (yellow) with CKS1 (pink). **(e)** Electrostatic surface potential of CKS1 revealing the binding of p27 phosphorylated Thr187 in a positively charged pocket and Pro188 in a hydrophobic groove **(f)** Ribbon diagram of p27 showing density (at 8.8σ , threshold 0.346) for the phosphorylated Thr187 protruding into CKS1 whilst p27 Pro188 stacks over CKS1 Tyr8 and is wedged by CKS1 Gln5 and Gln49.

Leu214, Trp217, Arg250, Leu253 and Gly251, (Fig. 3a,b), which also constitute van der Waals contacts with the p27 Leu-Phe pair. Following the LFG sequence, p27 forms an α -helix which rests over the α -5-helix of cyclin A (residues 288–301) and extends towards CDK2 (Fig. 3a,c) (PDB 1JSU).

Consistent with PDB 1JSU, we observe the β -hairpin of p27 (residues 60–71) packing against the N-terminal β -sheet of CDK2 to bury a cluster of aromatic residues, namely the conserved CIP/KIP residues Trp60, Phe64, Phe62, Tyr74 and Trp76 (Fig. 3c). Additionally, CDK2 Tyr77 hydrogen bonds with p27 Phe64 to stabilise the interaction. At the second region of the p27-CDK2 interface, the p27 β -strand (residues 75–81) forms a hybrid β -sheet with CDK2 (Fig. 3d), creating an interface that is dictated by hydrogen bonds between p27 Gln77 and CDK2 Lys20, and p27 Val79 and CDK2 Val18. Consistent with the crystal structure PDB 1JSU, we were unable to

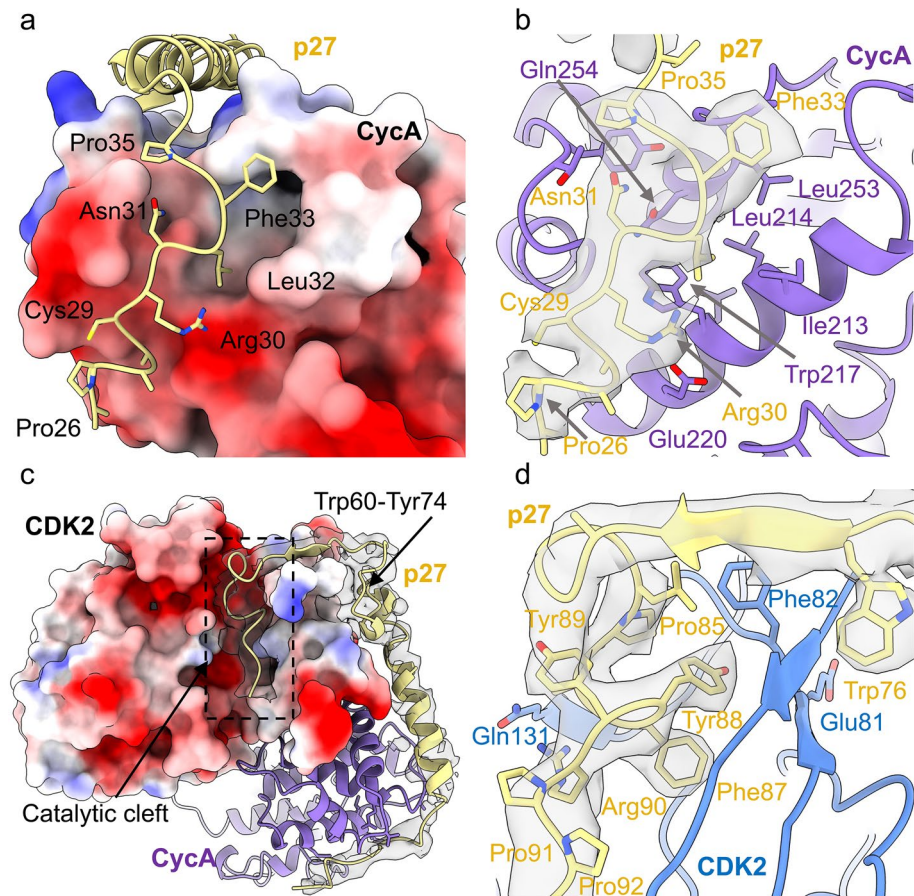


Figure 3. Binding of p27 with cyclin A and CDK2. (a,b) Interaction of p27 (yellow) with cyclin A (purple). (a) Electrostatic surface potential of cyclin A revealing binding of the p27 N-terminus in a shallow groove along the cyclin box repeat. The conserved p27 Leu-Phe-Gly sequence binds in a deeper, more hydrophobic groove. (b) Ribbon and density (at 6.0σ , threshold 0.205) diagram of p27 binding to the α -helices of the cyclin box repeat of cyclin A, where residues Ala28, Arg30 and Asn31 of p27 form hydrogen bonds with Trp127, Glu220 and Gln254 of cyclin A respectively. (c,d) Binding of p27 (yellow) with CDK2 (blue). (c) Electrostatic surface potential of CDK2 showing how p27 (density at 6.0σ , threshold 0.221) extends over CDK2 into the catalytic cleft, with residues Trp60, Phe64, Phe62, Tyr74 and Trp76 of p27 interacting with CDK2 (d) p27 3_{10} helix (residues 85–93) binds through the catalytic cleft of CDK2 and into the ATP binding site where p27 Tyr88 hydrogen bonds with the backbone of CDK2 Glu81 (density map at 8.8σ , threshold 0.315).

model the first β -strand of CDK2 (residues 1–13), suggesting it is disordered in solution upon p27 binding. The final component of the p27-CDK2 interaction involves the p27 3_{10} helix (residues 85–93), which binds through the catalytic cleft of CDK2 into the ATP binding site (Fig. 3d). This interaction is well conserved with the crystal structure (PDB [1JSU](#)) and highlights that p27 Tyr88 secures the binding by forming hydrogen bonds with CDK2 Glu81 and Leu83, and making van der Waals contacts with CDK2 Phe82 and Leu83 (Fig. 3d). Additionally, we were able to identify other key p27 residues; Phe87 sits deep in the active site cleft wedged by CDK2 residues Lys33, Leu134, Ala144 and Phe80, whilst p27 Arg90 hydrogen bonds with CDK2 Gln131 (Fig. 3d).

In general, the binding of p27 in the hexameric complex is broadly consistent with PDB [1JSU](#) and PDB [7B5R](#). However, all structures exhibit varying helical conformations of the KID as it extends towards the N-terminal lobe of CDK2 (Fig. 4). This supports analysis by Lacy and colleagues⁵² in which p27 was found to be dynamic, transitioning from disordered to nascent secondary structure on target binding, which may have implications for molecular recognition.

3D variability analysis reveals hinge motion within the hexameric complex. Given the inherent flexibility of the constituent components, we utilised 3D variability analysis⁵⁴ to visualise the conformational space of the hexameric complex. This analysis revealed a “breathing” motion in which p27 bound to cyclin A moves inwards and outwards from the SKP2 and SKP1 domains using CKS1 as a hinge point (Fig. 5, Supplementary: hexamer.mov S1). In the closed conformation the average distance between cyclin A and SKP1 is ~ 8 Å, whilst in the open conformation the average distance is ~ 16 Å (Fig. 5a,b). This motion is also reflected in the p27 KID, which concertedly moves with cyclin A as the complex transitions from closed to open, further supporting

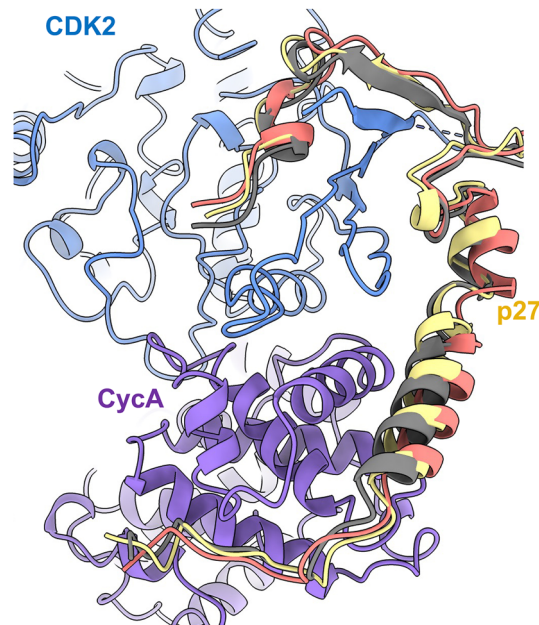


Figure 4. Helical conformation of p27 KID bound to CDK2-cyclin A. The CDK2, cyclin A and p27 subunits of the hexameric complex are shown in blue, purple and yellow respectively. The CDK2-cyclin A modules of CDK2-cyclin A-p27 (PDB **1JSU** (grey)) and the octameric SCF^{SKP2} E3 ligase structure (PDB **7B5R** (salmon)) were superposed with the hexameric CDK2-cyclin A module, and the p27 domains rendered in grey (PDB **1JSU**), salmon (PDB **7B5R**) and yellow (hexameric complex) respectively, to reveal different helical conformations for p27 KID when bound to CDK2-cyclin A.

its flexibility. Although less significant, some motion was also identified in SKP1, which concomitantly extends away from cyclin A.

On comparison, it is evident that the octameric SCF^{SKP2} E3 ligase structure (PDB **7B5R**) falls within the broad conformational space of the hexamer (Fig. 5c,d), suggesting the complex is generally unperturbed by CUL1. Whilst the octameric complex does not align directly with the open or closed conformation, it is most consistent with the closed form, with an average distance of ~10 Å between SKP1 and cyclin A (Fig. 5c,d). This analysis suggests a model in which p27 binding to CDK2-cyclin A-CKS1 generates a flexible substrate which, as it transitions between open and closed conformations, can be captured in a conformation that promotes recognition by SCF^{SKP2}. This motion is typical of the large structural rearrangements often required to bring the E2 and substrate together within the cullin-RING ligase complex⁵⁵. In the case of p27, the SKP2 substrate recognition motif is the limiting component in ubiquitin-mediated degradation²⁷. We speculate the observed motion may facilitate p27 recognition by bringing the substrate towards the SKP2 recognition component. This motion may also enhance p27 ubiquitination by shortening the E2-substrate distance for initiation of ubiquitination in the closed conformation; or in the open form, increase the space at the heart of the complex to assist the catalytic cycle. However, this study is limited in its biochemical scope to elucidate the functional importance of this motion beyond speculation. Future efforts could focus on evaluating the conformational space of the pentameric CDK2-cyclin A-CKS1-SKP1-SKP2 complex to determine if this flexibility profile exists in the absence of p27.

Particle subtraction identifies further features of the hexameric complex. In light of the 3D variability analysis, we performed particle subtraction and local refinement of the SKP1-SKP2-CKS1 (PDB **8BYL**, EMD-**16327**) and CDK2-cyclin A-p27 (PDB **8BZO**, EMD-**16344**) portions of the complex in an effort to improve the local resolution (Supplementary Fig. S5).

Following subtraction of the SKP1-SKP2-CKS1 signal and local refinement of CDK2-cyclinA-p27, the resolution of cyclin A was improved from 4.5–5.0 Å to 3.5–4.0 Å (compare Fig. 1c and Fig. 6a). Concomitant improvements throughout the p27 KID (Fig. 6a) were also observed, permitting modelling of side chains that previously could not be discerned (Supplementary Fig. S6a,b). Using the opposing strategy of subtracting signal for CDK2-cyclin A-p27 and refining SKP1-SKP2-CKS1 (PDB **8BYL**, EMD-**16327**), the resolution of CKS1, the bound p27 C-terminus, and the LRR domain and N-terminus of SKP2 were all improved (compare Fig. 1c with Fig. 6b). The most drastic improvement was observed in SKP1, in which the resolution was enhanced from 5–6 Å to 3.5–5.5 Å (Fig. 6b), allowing previously unmodelled residues in loop 2 (residues 64–71) (Fig. 6c) and loop 1 (residues 31–41) to be observed. However, the full length of loop 1 could not be modelled and comparison with the octameric complex (PDB **7B5R**) suggests this region of SKP1 forms part of the interface with CUL1 and may rigidify on CUL1 binding.

Local refinement of SKP1-SKP2-CKS1 provided opportunities for further modelling in SKP2 and C-terminus of p27. In the full hexameric map, the first observable SKP2 residue was Val95, whilst Pro93 and Gly94 could

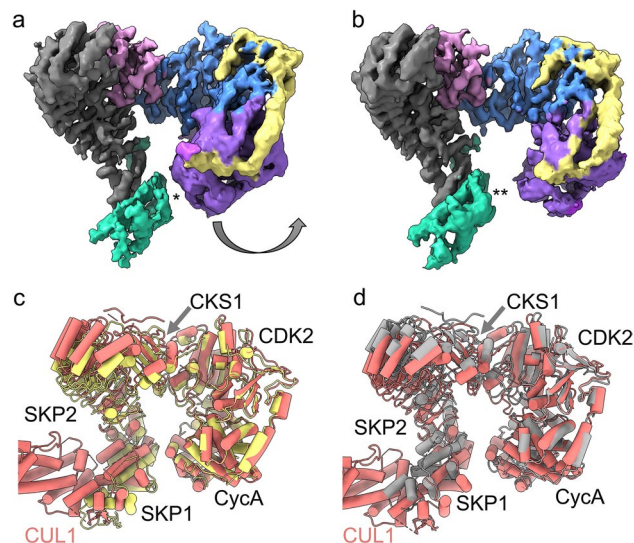


Figure 5. 3D variability analysis of the hexameric complex. **(a,b)** Cryo-EM maps representing the **(a)** closed conformation and **(b)** open conformation of the hexameric complex as revealed by 3D variability analysis. Cyclin A (purple) bound to p27 (yellow) swings away from N-terminal SKP2 (grey) and SKP1 (green) motif whilst the SKP1 domain concomitantly extends away from the cyclin A-p27 unit. Average distance between SKP1 and cyclin A is ~ 8 Å in closed conformation (as indicated by *) and ~ 16 Å in open conformation (as indicated by **). **(c,d)** Comparison of the octameric complex PDB **7B5R** with the open and closed conformations of the hexameric complex. Superposition of PDB **7B5R** (salmon) with the **(a)** closed conformation (yellow) and **(b)** open conformation (grey) of the hexameric complex showing that **7B5R** falls within the broad conformational space of the hexameric complex. The average distance between SKP1 and cyclin A is ~ 10 Å in PDB **7B5R**.

be modelled in the particle subtraction map, providing additional N-terminal residues not reported in the crystal structure (PDB **2AST**). This marginally improved N-terminal coverage on local refinement lends some weight to the N-terminus of SKP2 being disordered in the absence of cyclin A binding. Owing to the enhanced resolution of the SKP2-CKS1 junction, density for the bound p27 C-term peptide was also improved to a resolution ~ 3.0 – 3.5 Å (Fig. 6b). This permitted backbone modelling of additional residues (Gly177, Ser178, Pro179 and Asn180) that extend back towards the LRR of SKP2 (Fig. 6d) with p27 Gly182 protruding over SKP2. An overlay with structures PDB **2AST** and **7B5R** suggests some divergence in the conformation of this p27 peptide, however, our particle subtraction map suggests a condensed, potential helical conformation (Supplementary Fig. S7).

Using cryo-EM, we provide an in-depth structural analysis of the quaternary architecture of the CDK2-cyclin A-CKS1-SKP1-SKP2-p27 complex which forms part of the SCF^{SKP2} E3 ligase that controls p27 ubiquitin-mediated degradation. Our experimentally determined structure supports existing crystal structures of CDK2-cyclin A-p27³⁹ and SKP1-SKP2-CDK1-p27 peptide⁴⁰ complexes, whilst utilising the power of cryo-EM to highlight previously unidentified dynamic behaviour. Through 3D-variability analysis, we report significant structural flexibility that gives rise to open and closed conformations of the hexameric complex. It remains to be determined whether the hexamer retains this flexibility upon binding of CUL1 and RBX1, or whether incorporation into the octameric complex or the SCF-RBR E3-E3 super-assembly selects compatible hexamer conformational states. From either model it can be hypothesized that the ability of CKS1 to act as a hinge point may promote p27 regulation by SCF^{SKP2} through facilitating p27 recognition and ubiquitination. More broadly, we demonstrate the influence that the combined use of 3D-variability analysis and local refinement can have on particle clarity, which may be widely applicable to flexible protein complexes.

Materials and methods

Protein expression. Full-length human CDK2 was co-expressed with *S. cerevisiae* GST-CAK1 from a pGEX-6P-1 vector as a GST-fusion protein cleavable with 3C protease as described⁵⁶. The construct yields a CDK2 sequence preceded by Gly-Pro-Leu-Gly-Ser and is phosphorylated on Thr160 (T160pCDK2). Untagged human cyclin A2 (residues 174–432)⁵⁶ and full-length human His₆-CKS1⁵⁷ were expressed using the pET21d vector, and full-length GST-p27 (residues 1–198) was expressed from a modified pGEX-6P1 vector¹⁴. Full-length GST-SKP2 (3C cleavable) was expressed with full-length SKP1 from a modified pET3d backbone⁴⁶. The cloning strategy leaves Gly-Pro at the start of SKP2. All constructs were expressed in BL21-DE3 (pLYS-S) cells grown at 30 °C in LB media till OD₆₀₀ ~ 0.7 – 0.8 , induced with 0.2 mM IPTG and incubated for 16 h at 18 °C. Cell pellets were resuspended in HEPES buffered saline (mHBS, 20 mM Tris pH 7.6, 300 mM NaCl, 1 mM DTT) with 200 μM RNAase A, 200 μM DNAaseI, lysed by sonication and clarified by centrifugation.

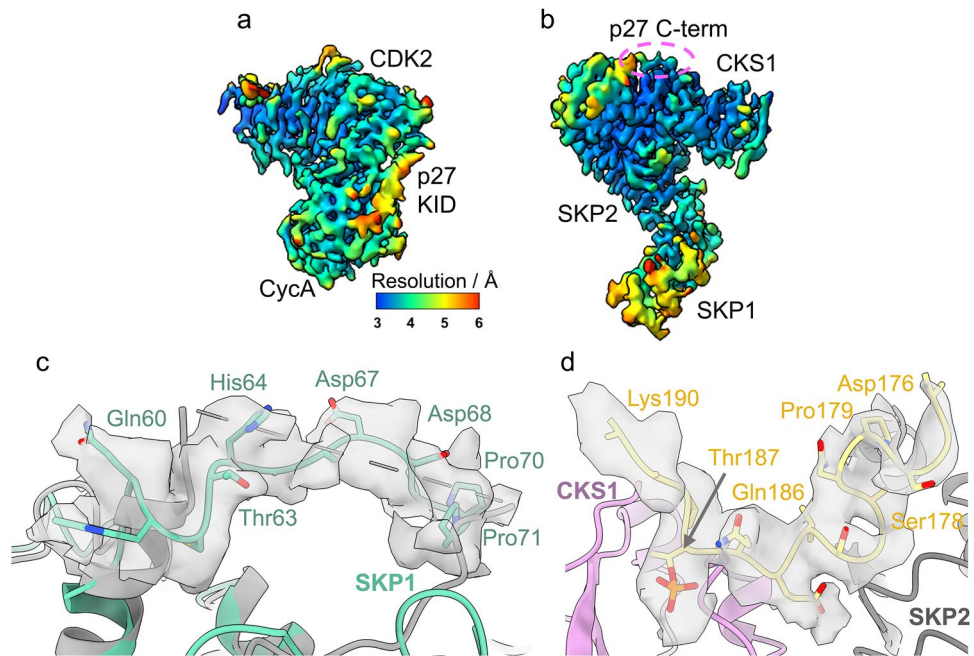


Figure 6. Local resolution analysis of particle subtraction maps. **(a,b)** Local resolution analysis of **(a)** particle subtraction map of CDK2-cyclin A-p27 (PDB **8BZO**, EMD-**16344**), showing enhanced resolution of the CDK2-cyclin A core and the KID of p27. **(b)** Particle subtraction map of SKP1-SKP2-CKS1 (EMD-**16327**, PDB **8BYL**) demonstrating improved resolution in the SKP1 domain and the phosphorylated C-terminus of p27 bound to CKS1 (circled in pink). **(c)** Particle subtraction and local refinement of SKP1-SKP2-CKS1, density (depicted at 4.0σ , threshold 0.110) yields an improvement in map continuity and resolution for SKP1 loop 2 which was not observed in the full hexameric model (grey, as indicated by dotted linker). **(d)** Improvement of density (at 3.2σ , threshold 0.143) for the C-terminus of p27 bound over CKS1 allows previously unobserved residues Asp176, Gly177, Ser178, Pro179 and Asn180 to be modelled extending towards the LRR of SKP2.

Protein purification. The SKP1-SKP2 complex and p27 were purified by affinity chromatography on a glutathione-sepharose column (Merck) equilibrated in mHBS as described previously⁴⁶. Proteins were eluted by 20 mM glutathione in mHBS pH 8.0, cleaved with 3C protease (1:50 w/w) and further purified using size exclusion chromatography (SEC) (Superdex 200 HR 16/60 (Cytiva)) equilibrated in 20 mM Tris pH 7.8, 300 mM NaCl, 0.5 mM TCEP. T160pCDK2-cyclin A complex was prepared as previously described⁵⁶. Briefly, a glutathione-sepharose column equilibrated in mHBS was charged with GST-T160pCDK2, washed to baseline and then used as an affinity column to purify untagged cyclin A. After washing to baseline T160pCDK2-cyclin A was eluted with 20 mM glutathione in mHBS, cleaved with 3C protease and subjected to SEC (Superdex 200 HR 16/60 (Cytiva)) equilibrated in 20 mM Tris pH 7.8, 300 mM NaCl, 0.5 mM TCEP. Co-eluting GST dimer was removed through subtractive GST. CKS1 was purified by affinity chromatography on a HiTrap His column (Cytiva) equilibrated in 40 mM HEPES pH 7.0, 200 mM NaCl, 25 mM imidazole and eluted with a gradient of 300 mM imidazole before loading onto a Superdex75 column (Cytiva) equilibrated in 20 mM Tris pH 7.8, 300 mM NaCl, 0.5 mM TCEP. The His6 tag was not cleaved.

Phosphorylation of p27 T187 and hexameric assembly. T160pCDK2-cyclinA-p27 (5.3 mg) in 40 mM Tris-HCl (pH 7.6), 1 mM ATP, 10 mM MgCl₂ buffer was incubated with 4.2 mg of T160pCDK2-cyclin A in a total volume of 2 mL at 25 °C for 2 h. The reaction mix was loaded on to a Superdex 200 16/60 HR column (Cytiva) equilibrated in 20 mM Tris pH 7.8, 300 mM NaCl, 0.5 mM TCEP buffer to remove the T160pCDK2-cyclin A. To assemble the complex, equimolar concentrations of purified CDK2-cyclinA-p27 (phosphorylated on CDK2 T160 and p27 T187) and SKP1-SKP2 complexes were incubated with a molar excess of CKS1 for 1 h at 4 °C and separated by SEC on a Superdex 200 10/300 column (Cytiva) equilibrated in 20 mM Tris pH 7.8, 300 mM NaCl, 0.5 mM TCEP.

Data collection. Particle distribution was assessed by analysis of negatively stained samples using uranyl acetate on a 120 kV microscope (Hitachi TS8700). The complex was subsequently loaded on 400-mesh Ultra-Foil R1.2/1.3 (Quantifoil) grids cleaned using Tergeo-EM plasma cleaner (PIE Scientific) for 1 min in remote plasma generated by an RF power (W) of 15, pulse ratio of 255, using a mixture of nitrogen, oxygen and argon. 3 μ l of hexameric complex (0.2 mg/ml) were blotted on the grids for 6 s with a blot force of -6 using a Vitrobot MK IV (Thermo Fisher Scientific) operated at 95% humidity at 5 °C. The grids were vitrified in liquid ethane and screened on a Titan Krios microscope (Thermo Fisher Scientific) operating at 300 kV with an energy-filtered K2 direct detector with an energy filter set with a 20 eV slit width (Gatan). Data acquisition was setup using EPU

software (Thermo Fisher Scientific). 762 electron movies were recorded at 130 k magnification in counting mode with a pixel size of 1.07 Å and a total dose of 65.8 e/Å². Data were collected at – 1.0 to – 3.0 µm defocus.

Hexameric complex data processing. All data were processed in CryoSPARC⁵⁸ following the workflow outlined in Supplementary Fig. S2.

Micrograph correction, autopicking and map generation. 762 movies were motion corrected using Patch Motion Correct Multi and the contrast transfer function (CTF) parameters were estimated using Patch CTF Correction Multi. Exposures were curated to remove poor micrographs and the remaining 673 micrographs were used for particle picking using blob picker with a minimum and maximum particle diameter of 70 Å and 160 Å. 1,110,356 particles were picked, extracted with a box size of 300 px (Fourier cropped to 150 px) and 2D classified. After discarding poor particles, 438,448 particles were used to generate 2D templates low pass filtered to 20 Å for template picking.

613,930 template picked particles were subjected to two rounds of 2D classification and the remaining 246,303 particles were used to generate a single ab-initio model that was refined through the homogenous refinement. 50 × 2D templates were generated from the refined map and used for template picking of 669,988 particles. These particles were extracted with a box size of 300 px (Fourier cropped to 150 px) and classified through 3 × 2D classification to yield 217,628 particles. These particles were re-extracted without Fourier cropping and 3D classified using heterogenous refinement. The particles were sorted into 3 × 3D classes, yielding class 2 with best map of 136,325 particles (5.14 Å). This class was refined through homogenous refinement and non-uniform refinement⁵⁹ to yield the final map at 3.4 Å resolution (FSC cut off 0.143). The final map was sharpened using a B-factor of – 121 Å², as indicated by the Guinier plot, and local resolution was estimated.

3D variability analysis, particle subtraction and local refinement. 3D variability analysis⁵⁴ was performed on the final 136,325 particle set, using a mask that encompassed the full complex, solving for 3 orthogonal principal modes over 20 iterations with a 5 Å resolution filter. The first and last frames were captured to depict the closed and open conformations of the hexamer respectively.

Using the full hexameric map, a mask for the SKP1-SKP2-CKS1 portion of the complex was generated in UCSF ChimeraX^{41,42} and low pass filtered to 20 Å with additional dilation (radius of 5) and padding (soft padding width 16) in CryoSPARC via the volume tools function. This mask was used to subtract signal of the SKP1-SKP2-CKS1 from the particles. Signal subtracted particles were refined using local refinement with a mask (low pass filter 20 Å, dilation radius 5 and soft padding width 16) generated from the CDK2-cyclinA-p27 portion of the complex. The reverse processing of subtracting CDK2-cyclinA-p27 signal and refining the SKP1-SKP2-CKS1 portion was performed to yield two subcomplex maps.

Model docking, refinement and validation. Initial rigid body docking of subdomains of the hexameric complex was performed in UCSF ChimeraX^{41,42} using CDK2-cyclinA-p27 (PDB [1JSU](#)) SKP1-SKP2-CKS1-p27 (PDB [2AST](#)). The maps were imported into Phenix⁶⁰ for subsequent model refinement and validation^{61,62}. The fitting of this model was improved with Real-space refinement⁴³ followed by manual refinement in COOT⁴⁴ based on the MolProbity⁶¹ outlines. The model quality was assessed in Phenix using Comprehensive Validation⁶² before deposition to the Protein Data Bank (PDB) and the Electron Microscopy Data Bank (EMDB).

Data availability

The map and model of the hexameric CDK2-cyclin A-CKS1-p27-SKP1-SKP2 complex has been deposited in the Protein Data Bank and the Electron Microscopy Data Bank with accession numbers [8BYA](#), and [16325](#) respectively. The particle subtraction maps and models for SKP1-SKP2-CKS1 and CDK2-Cyclin A-p27 are deposited with accession codes PDB [8BYL](#)/EMD-[16327](#) and PDB [8BZO](#)/EMD-[16344](#) respectively.

Received: 18 May 2023; Accepted: 24 June 2023

Published online: 03 July 2023

References

- Morgan, D.O. The cell cycle principles of control. In *Primers in Biology* (New Science Press Ltd, 2007).
- Gopinathan, L., Ratnacaram, C. K. & Kaldis, P. Established and novel Cdk/Cyclin complexes regulating the cell cycle and development. *Res. Probl. Cell Differ* **1**, 365–389. https://doi.org/10.1007/978-3-642-19065-0_16 (2011).
- Malumbres, M. Cyclin-dependent kinases. *Genome Biol.* **15**, 122. <https://doi.org/10.1186/gb4184> (2014).
- Suski, J. M. *et al.* CDC7-independent G1/S transition revealed by targeted protein degradation. *Nature* **605**, 357–365. <https://doi.org/10.1038/s41586-022-04698-x> (2022).
- Wood, D. J. & Endicott, J. A. Structural insights into the functional diversity of the CDK–cyclin family. *Open Biol.* **8**, 180112. <https://doi.org/10.1098/rsob.180112> (2018).
- Koliopoulos, M. G. & Alfieri, C. Cell cycle regulation by complex nanomachines. *FEBS J.* **289**, 5100–5120. <https://doi.org/10.1111/febs.16082> (2022).
- Nakayama, K. I. K. & Nakayama, K. I. K. Ubiquitin ligases: Cell-cycle control and cancer. *Nat. Rev. Cancer.* **6**, 369–381. <https://doi.org/10.1038/nrc1881> (2006).
- Sherr, C. J. & Roberts, J. M. CDK inhibitors: Positive and negative regulators of G1-phase progression. *Genes Dev.* **13**, 1501–1512. <https://doi.org/10.1101/gad.13.12.1501> (1999).
- Soos, T. J. *et al.* Formation of p27-CDK complexes during the human mitotic cell cycle. *Cell Growth Differ.* **7**, 135–146 (1996).
- LaBaer, J. *et al.* New functional activities for the p21 family of CDK inhibitors. *Genes Dev.* **11**, 847–862. <https://doi.org/10.1101/gad.11.7.847> (1997).

11. Blain, S. W., Montalvo, E., Massagué, J. & Massague, J. Differential interaction of the cyclin-dependent kinase (Cdk) inhibitor p27Kip1 with Cyclin A-Cdk2 and Cyclin D2-Cdk4. *J. Biol. Chem.* **272**, 25863–25872. <https://doi.org/10.1074/jbc.272.41.25863> (1997).
12. Cheng, M. *et al.* The p21(Cip1) and p27(Kip1) CDK “inhibitors” are essential activators of cyclin D-dependent kinases in murine fibroblasts. *EMBO J.* **18**, 1571–1583. <https://doi.org/10.1093/emboj/18.6.1571> (1999).
13. Larrea, M. D. *et al.* Phosphorylation of p27 Kip1 regulates assembly and activation of cyclin D1–Cdk4. *Mol. Cell Biol.* **28**, 6462–6472. <https://doi.org/10.1128/MCB.02300-07> (2008).
14. Hallett, S. T. *et al.* Differential regulation of G1 CDK complexes by the Hsp90–Cdc37 Chaperone system. *Cell Rep.* **21**, 1386–1398. <https://doi.org/10.1016/j.celrep.2017.10.042> (2017).
15. Sherr, C. J., Beach, D. & Shapiro, G. I. Targeting CDK4 and CDK6: From discovery to therapy. *Cancer Discov.* **6**, 353–367. <https://doi.org/10.1158/2159-8290.CD-15-0894> (2016).
16. Polyak, K. *et al.* Cloning of p27Kip1, a cyclin-dependent kinase inhibitor and a potential mediator of extracellular antimetastatic signals. *Cell* **78**, 59–66. [https://doi.org/10.1016/0092-8674\(94\)90572-X](https://doi.org/10.1016/0092-8674(94)90572-X) (1994).
17. Polyak, K. *et al.* p27Kip1, a cyclin-Cdk inhibitor, links transforming growth factor-beta and contact inhibition to cell cycle arrest. *Genes Dev.* **8**, 9–22 (1994).
18. Harvat, B. L., Seth, P. & Jetten, A. M. The role of p27Kip1 in gamma interferon-mediated growth arrest of mammary epithelial cells and related defects in mammary carcinoma cells. *Oncogene* **14**, 2111–2122. <https://doi.org/10.1038/sj.onc.1201055> (1997).
19. Hu, X. T. & Zuckerman, K. S. Role of cell cycle regulatory molecules in retinoic acid- and vitamin D3-induced differentiation of acute myeloid leukaemia cells. *Cell Prolif.* **47**, 200–210. <https://doi.org/10.1111/cpr.12100> (2014).
20. Mayor, S. Protein marker linked with poor cancer outcome. *BMJ* **314**, 323–323. <https://doi.org/10.1136/bmj.314.7077.323a> (1997).
21. Loda, M. *et al.* Increased proteasome-dependent degradation of the cyclin-dependent kinase inhibitor p27 in aggressive colorectal carcinomas. *Nat. Med.* **3**, 231–234. <https://doi.org/10.1038/nm0297-231> (1997).
22. Pagano, M. *et al.* Role of the ubiquitin-proteasome pathway in regulating abundance of the cyclin-dependent kinase inhibitor p27. *Science* **269**(1995), 682–685. <https://doi.org/10.1126/science.7624798> (1979).
23. Shirane, M. *et al.* Down-regulation of p27 by two mechanisms, ubiquitin-mediated degradation and proteolytic processing. *J. Biol. Chem.* **274**, 13886–13893. <https://doi.org/10.1074/jbc.274.20.13886> (1999).
24. Sheaff, R. J., Groudine, M., Roberts, J. M. Cyclin E-CDK2 is a regulator of p27 Kip1, 1464–1478 (1997).
25. Vlach, J., Hennecke, S. & Amati, B. Phosphorylation-dependent degradation of the cyclin-dependent kinase inhibitor p27Kip1. *EMBO J.* **16**, 5334–5344. <https://doi.org/10.1093/emboj/16.17.5334> (1997).
26. Montagnoli, A. *et al.* Ubiquitination of p27 is regulated by Cdk-dependent phosphorylation and trimeric complex formation. *Genes Dev.* **13**, 1181–1189. <https://doi.org/10.1101/gad.13.9.1181> (1999).
27. Carrano, A. C., Eytan, E., Hershko, A. & Pagano, M. SKP2 is required for ubiquitin-mediated degradation of the CDK inhibitor p27. *Nat. Cell Biol.* **1**, 193–199. <https://doi.org/10.1038/12013> (1999).
28. Sutterlüty, H. *et al.* p45SKP2 promotes p27Kip1 degradation and induces S phase in quiescent cells. *Nat. Cell Biol.* **1**, 207–214. <https://doi.org/10.1038/12027> (1999).
29. Tsvetkov, L. M., Yeh, K. H., Lee, S. J., Sun, H. & Zhang, H. p27(Kip1) ubiquitination and degradation is regulated by the SCF(Skp2) complex through phosphorylated Thr187 in p27. *Curr. Biol.* **9**, 661–664 (1999).
30. Xu, S. *et al.* Substrate recognition and ubiquitination of SCFSkp2/Cks1 ubiquitin-protein isopeptide ligase. *J. Biol. Chem.* **282**, 15462–15470. <https://doi.org/10.1074/jbc.M610758200> (2007).
31. García-Gutiérrez, L. *et al.* Myc stimulates cell cycle progression through the activation of Cdk1 and phosphorylation of p27. *Sci. Rep.* **9**, 18693. <https://doi.org/10.1038/s41598-019-54917-1> (2019).
32. Zhang, H., Kobayashi, R., Galaktionov, K. & Beach, D. p19skp1 and p45skp2 are essential elements of the cyclin A-CDK2 S phase kinase. *Cell* **82**, 915–925. [https://doi.org/10.1016/0092-8674\(95\)90271-6](https://doi.org/10.1016/0092-8674(95)90271-6) (1995).
33. Bai, C. *et al.* SKP1 connects cell cycle regulators to the ubiquitin proteolysis machinery through a novel motif, the F-Box. *Cell* **86**, 263–274. [https://doi.org/10.1016/S0092-8674\(00\)80098-7](https://doi.org/10.1016/S0092-8674(00)80098-7) (1996).
34. Cenciarelli, C. *et al.* Identification of a family of human F-box proteins. *Curr. Biol.* **9**, 1177–S3. [https://doi.org/10.1016/S0960-9822\(00\)80020-2](https://doi.org/10.1016/S0960-9822(00)80020-2) (1999).
35. Spruck, C. *et al.* A CDK-independent function of mammalian Cks1: targeting of SCF(Skp2) to the CDK inhibitor p27Kip1. *Mol. Cell.* **7**, 639–650 (2001).
36. Ganoth, D. *et al.* The cell-cycle regulatory protein Cks1 is required for SCF(Skp2)-mediated ubiquitinylation of p27. *Nat. Cell Biol.* **3**, 321–324. <https://doi.org/10.1038/35060126> (2001).
37. Sitry, D. *et al.* Three different binding sites of Cks1 are required for p27-ubiquitin ligation. *J. Biol. Chem.* **277**, 42233–42240. <https://doi.org/10.1074/jbc.M205254200> (2002).
38. Hao, B. *et al.* Structural basis of the Cks1-dependent recognition of p27(Kip1) by the SCF(Skp2) ubiquitin ligase. *Mol. Cell.* **20**, 9–19. <https://doi.org/10.1016/j.molcel.2005.09.003> (2005).
39. Russo, A. A., Jeffrey, P. D., Patten, A. K., Massague, J. & Pavletich, N. P. Crystal structure of the p27Kip1 cyclin-dependent-kinase inhibitor bound to the cyclin A-Cdk2 complex. *Nature* **382**, 325–331. <https://doi.org/10.1038/382325a0> (1996).
40. Hao, B. *et al.* Structural basis of the Cks1-dependent recognition of p27Kip1 by the SCFSkp2 Ubiquitin ligase. *Mol. Cell.* **20**, 9–19. <https://doi.org/10.1016/j.molcel.2005.09.003> (2005).
41. Goddard, T. D. *et al.* Meeting modern challenges in visualization and analysis. *Protein Sci.* **27**, 14–25. <https://doi.org/10.1002/pro.3235> (2018).
42. Pettersen, E. F. *et al.* UCSF ChimeraX: Structure visualization for researchers, educators, and developers. *Protein Sci.* **30**, 70–82. <https://doi.org/10.1002/pro.3943> (2021).
43. Afonine, P. V. *et al.* Real-space refinement in PHENIX for cryo-EM and crystallography. *Acta Crystallogr. D Struct. Biol.* **74**, 531–544. <https://doi.org/10.1107/S2059798318006551> (2018).
44. Emsley, P. & Cowtan, K. Coot: Model-building tools for molecular graphics. *Acta Crystallogr D.* **60**, 2126–2132. <https://doi.org/10.1107/S0907444904019158> (2004).
45. Ji, P. *et al.* Skp2 contains a novel cyclin binding domain that directly protects cyclin A from inhibition by p27Kip1. *J. Biol. Chem.* **281**, 24058–24069. <https://doi.org/10.1074/jbc.M603105200> (2006).
46. Salamina, M. *et al.* Discriminative SKP2 interactions with CDK-cyclin complexes support a cyclin A-specific role in p27KIP1 degradation. *J. Mol. Biol.* **433**, 166795. <https://doi.org/10.1016/j.jmb.2020.166795> (2021).
47. Kelso, S. *et al.* Bipartite binding of the N terminus of Skp2 to cyclin A. *Structure.* **29**, 975–988.e5. <https://doi.org/10.1016/j.str.2021.04.011> (2021).
48. Horn-Ghetko, D. *et al.* Ubiquitin ligation to F-box protein targets by SCF-RBR E3–E3 super-assembly. *Nature* **590**, 671–676. <https://doi.org/10.1038/s41586-021-03197-9> (2021).
49. Schulman, B. A. *et al.* Insights into SCF ubiquitin ligases from the structure of the Skp1–Skp2 complex. *Nature* **408**, 381–6. <https://doi.org/10.1038/35042620> (2000).
50. Kachariya, N. N., Dantu, S. C. & Kumar, A. Backbone and side chain assignments of human cell cycle regulatory protein S-phase kinase-associated protein 1. *Biomol. NMR Assign.* **10**, 351–355. <https://doi.org/10.1007/s12104-016-9699-2> (2016).
51. Tsytlonok, M. *et al.* Specific conformational dynamics and expansion underpin a multi-step mechanism for specific binding of p27 with Cdk2/Cyclin A. *J. Mol. Biol.* **432**, 2998–3017. <https://doi.org/10.1016/j.jmb.2020.02.010> (2020).

52. Lacy, E. R. *et al.* p27 binds cyclin-CDK complexes through a sequential mechanism involving binding-induced protein folding. *Nat. Struct. Mol. Biol.* **11**, 358–364. <https://doi.org/10.1038/nsmb746> (2004).
53. Bourne, Y. *et al.* Crystal structure and mutational analysis of the human CDK2 kinase complex with cell cycle-regulatory protein CksHs1. *Cell* **84**, 863–874. [https://doi.org/10.1016/S0092-8674\(00\)81065-X](https://doi.org/10.1016/S0092-8674(00)81065-X) (1996).
54. Punjani, A. & Fleet, D. J. 3D variability analysis: Resolving continuous flexibility and discrete heterogeneity from single particle cryo-EM. *J Struct Biol.* **213**, 107702. <https://doi.org/10.1016/j.jsb.2021.107702> (2021).
55. Harper, J. W. & Schulman, B. A. Cullin-RING ubiquitin ligase regulatory circuits: A quarter century beyond the F-Box hypothesis. *Annu. Rev. Biochem.* **90**, 403–429. <https://doi.org/10.1146/annurev-biochem-090120-013613> (2021).
56. Brown, N. R., Noble, M. E. M., Endicott, J. A. & Johnson, L. N. The structural basis for specificity of substrate and recruitment peptides for cyclin-dependent kinases. *Nat. Cell Biol.* **1**, 438–443. <https://doi.org/10.1038/15674> (1999).
57. Brown, N. R. *et al.* CDK1 structures reveal conserved and unique features of the essential cell cycle CDK. *Nat. Commun.* **6**, 6769. <https://doi.org/10.1038/ncomms7769> (2015).
58. Punjani, A., Rubinstein, J. L., Fleet, D. J. & Brubaker, M. A. cryoSPARC: Algorithms for rapid unsupervised cryo-EM structure determination. *Nat. Methods.* **14**, 290–296. <https://doi.org/10.1038/nmeth.4169> (2017).
59. Punjani, A., Zhang, H. & Fleet, D. J. Non-uniform refinement: adaptive regularization improves single-particle cryo-EM reconstruction. *Nat. Methods.* **17**, 1214–1221. <https://doi.org/10.1038/s41592-020-00990-8> (2020).
60. Liebschner, D. *et al.* Macromolecular structure determination using X-rays, neutrons and electrons: Recent developments in Phenix. *Acta Crystallogr. D Struct. Biol.* **75**, 861–877. <https://doi.org/10.1107/S2059798319011471> (2019).
61. Williams, C. J. *et al.* MolProbity: More and better reference data for improved all-atom structure validation. *Protein Sci.* **27**, 293–315. <https://doi.org/10.1002/pro.3330> (2018).
62. Afonine, P. V. *et al.* New tools for the analysis and validation of cryo-EM maps and atomic models. *Acta Crystallogr. D Struct. Biol.* **74**, 814–840. <https://doi.org/10.1107/S2059798318009324> (2018).

Acknowledgements

This research was supported by the Medical Research Council (Grant References MR/N009738/1 and MR/V029142/1). Cryogenic electron microscopy was carried out at the York Structural Biology Lab (Wellcome Trust grant number 206161/Z/17/Z) and Leeds Astbury Centre. At the University of Leeds, the FEI Titan Krios microscopes were funded by the University of Leeds (UoL ABSL award) and The Wellcome Trust (108466/Z/15/Z), with Falcon 4 and Selectris Falcon4 direct electron detector and microED packages (Q2 2021) upgrades funded by The Wellcome Trust (221524/Z/20/Z). We would like to thank S. Lea, D. Elmlund and H. Elmlund for their assistance during initial stages of this project. For the purpose of open access, the authors have applied a Creative Commons Attribution (CC BY) licence to any Author Accepted Manuscript version arising from this submission.

Author contributions

R.R.: conceptualization, cryo-EM data analysis, structure determination, investigation and writing (review and editing). R.H.: resources (construct design). D.M.: Cryo-EM data acquisition and analysis. R.T.: Cryo-EM data acquisition and analysis. N.R.: resources and funding acquisition. J.B.: Cryo-EM data acquisition. J.E.: conceptualization, resources, supervision, funding acquisition, writing (original draft, review and editing). M.N.: conceptualization, resources, supervision, funding acquisition, writing (original draft, review and editing). M.S.: conceptualization, collaboration, methodology (protein expression and purification), cryo-EM data collection and analysis, investigation and writing. All authors reviewed the manuscript.

Competing interests

M.S. and R.F.T are current employees of Evotec SE and Thermo Fisher Scientific respectively. The other authors declare no competing interests. The authors declare no competing financial interest. Some work in the authors' laboratory is supported by a research grant from Astex Pharmaceuticals.

Additional information

Supplementary Information The online version contains supplementary material available at <https://doi.org/10.1038/s41598-023-37609-9>.

Correspondence and requests for materials should be addressed to J.A.E. or M.S.

Reprints and permissions information is available at www.nature.com/reprints.

Publisher's note Springer Nature remains neutral with regard to jurisdictional claims in published maps and institutional affiliations.



Open Access This article is licensed under a Creative Commons Attribution 4.0 International License, which permits use, sharing, adaptation, distribution and reproduction in any medium or format, as long as you give appropriate credit to the original author(s) and the source, provide a link to the Creative Commons licence, and indicate if changes were made. The images or other third party material in this article are included in the article's Creative Commons licence, unless indicated otherwise in a credit line to the material. If material is not included in the article's Creative Commons licence and your intended use is not permitted by statutory regulation or exceeds the permitted use, you will need to obtain permission directly from the copyright holder. To view a copy of this licence, visit <http://creativecommons.org/licenses/by/4.0/>.

© The Author(s) 2023